Inorganic Chemistry Communications 160 (2024) 111933

Contents lists available at ScienceDirect

Inorganic Chemistry Communications

journal homepage: www.elsevier.com/locate/inoche

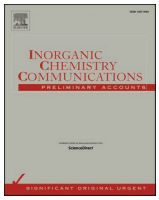

Short communication

In-situ Salen-type ligand formation-driven of a heterometallic Cu(II)-Hg(II) complex: Synthetic update, crystallographic features, DFT calculations, and unveil antimicrobial profiles

Dhrubajyoti Majumdar [a,*], Sourav Roy [b], Jessica Elizabeth Philip [c], Burak Tüzün [d], Suman Hazra [a]

[a] Department of Chemistry, Tamralipta Mahavidyalaya, Tamluk 721636, West Bengal, India
[b] Solid State and Structural Chemistry Unit, Indian Institute of Science, Bangalore 560012, India
[c] Department of Chemistry, Alphonsa College, Palai, Kottayam, Kerala 686574, India
[d] Sivas Cumhuriyet University, Sivas Vocational School, Department of Plant and Animal Production, TR-58140 Sivas, Turkey

ARTICLE INFO

Keywords:
Salen ligand
Cu(II)-Hg(II)
DFT
Molecular docking
PLIP
Antimicrobial

ABSTRACT

This article vividly describes the synthesis and structural characterization of one 6-Bromo-2-hydroxy-3-methoxybenzaldehyde ligand involving heteronuclear complex, $[Cu(L)Hg(Cl)_2]$. X-ray single-crystal determined the complex crystal structure and characterized it by various physical methods, including elemental, FT-IR, Raman, PXRD, UV–vis, NMR, and SEM-EDX techniques. X-ray diffraction analysis reveals that the compound adopts a monoclinic space group *Cc* during crystallization. The crystal structure exhibits unique supramolecular interactions, like intermolecular C-H•••π H-bonding and X-bonding (X = Halogen) between Br(1) and Br(2) atoms. Hirshfeld surfaces (HS) and 2-D fingerprint plots confirm significant H…Cl (21.9 %) contacts. Further, dispersion energy dominates due to Br atoms' higher electron/electron cloud. The complex underwent DFT calculations based on the Gaussian software package at B3LYP, HF, and M062x levels, utilizing the lanl2dz, sdd, and def2tzvp basis sets. The HOMO-LUMO, ESP, Global reactivity, Interaction energy and energy frameworks, and Fukui function investigated the complex properties in a multidimensional spectrum. The complex showed promising NLO activity, which has broad technological applications. Fukui function calculation identifies regions prone to nucleophilic (Nu^-) and electrophilic (E^+) attacks. The complex and synthetic components were examined for antimicrobial function against Gram+ve and Gram-ve bacterial and fungal strains. Molecular docking (MD) and Protein-Ligand Interaction Profilers (PLIP) further support the antimicrobial findings.

1. Introduction

In the current research scenario, there has been a surge in interest in the synthetic design of heteronuclear metal complexes due to their unique and attractive crystal structures [1]. Therefore, synthetic inorganic chemists have paid much attention to synthesizing hetero/homonuclear complex frameworks using N/O-donor compartmental Salen/Salen-type (Scheme S1) or even Salamo-Salen ligands in coordination chemistry [2–11]. Accordingly, triggering the coordination of two or more transition /post-transition metal ions (M^{n+}) to suitably designed binding sites of Salen-type ligands could result in self-assembled heteronuclear complex structural motifs [12]. These ligand complexes possess fascinating structural and magnetic properties, making them attractive [1]. The N_2O_4 Salen-type ligand may have an inner compartment of N_2O_2 and an outer compartment of O_4. It contains imines (–CH = N), alkoxy's (–OCH_3), and phenolic (–OH) groups (Scheme S2) [3,5,6]. All the donor centres are readily encapsulated homo/hetero-type metal ions in two different compartments forming hetero- and polynuclear metal complexes [3–6]. In addition, a growing research interest is observed in Cu(II) and Hg(II) metal ions and their complexes [13,14]. These metal complexes display diverse coordination chemistry and, together with their abundance and low cost, have wide-ranging applications [15]. Recently, researchers have been utilizing Cu(II)-Schiff base-based compounds in chemical processes due to the stimulation provided by the complexes [16]. Further, living organisms require Cu(II) ions for proper functioning, and the complexes formed by

* Corresponding author.
E-mail address: dmajumdar30@gmail.com (D. Majumdar).

https://doi.org/10.1016/j.inoche.2023.111933
Received 26 November 2023; Received in revised form 13 December 2023; Accepted 16 December 2023
Available online 18 December 2023

these ions have medicinal applications [15]. In addition, Cu(II) complexes can induce cancer cell death via DNA damage and reactive oxygen species (ROS) generation [17]. Hence, the research area of hetero and polynuclear Cu(II)-Schiff base complexes has been widespread and attractive to inorganic chemists [1–3,7,15,17]. Notably, the initial reports on dye-sensitized solar cell (DSSC) devices triggered research on Hg(II) complexes in this field because of the stable structure and intense luminescence properties yielded by the combination of d^{10} metals and Schiff base ligands [18]. Again, due to high toxicity, mercury metal (Hg) is considered one of the most hazardous heavy elements for animals and humans. HgX_2 (X = halide ions) tends to dimerize, forming a planar interesting HgX…XHg crystal structure [19,20]. Therefore, most scientists are interested in the environmental effects of mercury and search for newly synthesized metal complex crystal structures [1–3,15,16,21–25]. Today, in research contributions, scientists worldwide have utilized complex systems or metallogel containing various metal ions for cell imaging, photodynamic therapy, chemotherapy, and antibacterial activity [26]. In this context, synthetic chemists have increasingly utilized DFT methods to search as-prepared coordination complexes' novel and unique properties [15,17,27–34]. The studies cover the HS, HOMO-LUMO, ESP, Global reactivity parameters, NLO, Fukui function, and molecular docking (MD) [27,35–38]. FMO/ESP evaluates chemical reactivity in relevant metal complexes [17,39,40]. Compounds with NLO properties are crucial in various fields, and the synthesis of NLO active metal complexes has been applied in research on inorganic and organic semiconductors and polymer architecture [28,41]. As a result, exploring the NLO properties of the recently synthesized complex in this framework presents excellent potential [42]. There is a growing interest in searching the antimicrobial spectrum of Schiff base compounds, leading to the development of MD studies [43]. PLIP is essential in structural bioinformatics, drug discovery, and biology for studying protein–ligand interactions [3].

This report presents the crystal structure, structural characterization, and synthetic update of one new complex, $[Cu(L)Hg(Cl)_2]$. To investigate reactivity-based properties, we compute various quantum chemical parameters of the complex, like HS, FMO, ESP, NLO, and Fukui functions. The current efforts have demonstrated the complex's antibacterial and fungal activities against selected Gm + ve, Gm-ve, Bacterial, and fungal strains. MD and PLIP aim to investigate the relationship between the complex's theoretical and experimental antimicrobial efficacy.

2. Experimental

2.1. Materials and instrumentation

All the research chemicals utilized in this article must be of reagent grade. PerkinElmer offers elemental analysis services focused on CHN. FTIR spectra are collected usually using Perkin-Elmer Spectrum RX 1. Bruker RFS 27 as KBr pellets in the 4000–50 cm^{-1} range for Raman spectra. NMR spectra were performed on a Bruker FT-NMR spectrometer (within 400 MHz to 75.45 MHz). The model OXFORD XMX N analysed the EDX data. The SEM figures were investigated using the JEOL model (JSM-6390LV). The powder X-ray diffraction data was processed and analysed using the BRUKER AXS. The U-3501 spectrophotometer determines UV–visible spectra.

2.2. Bacterial/fungal cultures

The research compounds were tested to examine their effectiveness first for Staphylococcus aureus (ATCC 25923). After that, Bacillus subtilis (ATCC 6635), which are Gm + ve bacteria, as well as Pseudomonas aeruginosa (ATCC 27853) and Escherichia coli (ATCC 25922), which are Gm-ve strains like bacteria, and Candida albicans (ATCC 10231) and Aspergillus niger, which are fungi strains—the prepared compounds in vitro antibacterial and antifungal activity qualitatively evaluated based on Agar Well Diffusion process. The method of deciding MIC values using liquid broth involves serial dilutions—most strains are assembled from the American Type Culture Collection (ATCC) in Manassas, VA, USA, and especially procured from Himedia in India.

2.2.1. Maintenance of cultures

We used (vol/vol) 50 % glycerol (Himedia, Mumbai, India) to maintain the bacterial cultures and stored at −70 °C. The cultures were preserved on Trypticase Soy Agar (TSA; Difco Laboratories, Detroit, Mich USA)—the fungal Candida albicans and Aspergillus niger primarily cultured on Sabouraud Dextrose Agar (SDA) from Himedia.

2.3. Synthesis of ligand (H_2L)

Below is the prescribed synthetic protocol for the new Salen-type ligand [3]. 1,3-propanediamine (0.0371 g, 0.5 mmol) was dropwise mixed with 6-Bromo-2-hydroxy-3-methoxybenzaldehyde (0.231 g, 1 mmol) in 20 mL methanol solvent with constant stirring for about 30 min—then the solution mixture refluxing at four hours. After slow evaporation, the yellow ligand was allowed to solidify. The air-dried ligand was carefully collected. Yield: (88 %), Anal. Calc. for $C_{19}H_{20}Br_2N_2O_4$: C, 45.62; H, 4.03; N, 5.60 Found: C, 45.58; H, 4.0; N, 5.65 %. IR (KBr cm^{-1}) selected bands: ν(C = N), 1627, $\nu(C\text{-}O_{phenolic})$1235, ν(O–H), 2976, ^1H NMR (DMSO-d_6, 400 MHz): δ (ppm): 13.53 (s, 1H, OH), 8.73–8.68 (s, 1H, CH = N), 6.85–6.92 (m, 8H, Ar-H), 3.61–3.78 (t, 2H, N-CH_2), 2.08–2.51 (m, 2H, CH_2), ^{13}C NMR (DMSO-d_6, 75.45 MHz): δ (ppm): 114.78–149.49 (Arom-C), 157.56–165.42 (C-OH), 167.07 (CH = N), UV–Vis λ_{max} (CH_3OH): 215, and 243 nm.

2.4. Synthesis and crystallization of complex

Solid $CuCl_2{\cdot}2H_2O$ (0.171 g, 1 mmol) and $HgCl_2$ (0.272 g, 1 mmol) were mixed in a mortar after a proper pestle. Then, 20 mL methanol-dichloromethane solvent mixture (1:1, v/v) was dropwise added until the solid was dissolved, poured into the 16 mL Schiff base ligand solution, and stirred in a magnetic stirrer for two hours. The green solution was kept stirred at a constant temperature of 75 °C. The solution mixture was passed through a filter and slowly evaporated at room temperature. After ten days, we obtained needle-sized single crystals perfect for single-crystal X-ray diffraction. The crystals are washed and adequately air-dried. Yield: 0.425 g, (75 %), Anal. Calc. for $C_{19}H_{18}Br_2Cl_2CuHgN_2O_4$: C, 27.39; H, 2.18; N, 3.36; Cu, 7.63; Hg, 24.07 %. Found: C, 27.34; H, 2.22; N, 3.31; Cu, 7.58; Hg, 24.01 %. IR (KBr cm^{-1}) selected bands: ν(C = N), 1640, $\nu(C\text{-}O_{phenolic})$1209, ν(C–H), 2950–3370, ν(Cu–O), 600, ν(Cu–N), 789, FT-Raman (cm^{-1}) selected bands: ν(C = N), 1620, $\nu(C\text{-}O_{phenolic})$ 1225, ν(Ar-O),1460, ν(C–H), 2849–2995, ν(Cu–O), 631, ν(Cu–N), 745, ^1H NMR (DMSO-d_6, 400 MHz): δ (ppm): 8.27 (CH = N), 6.25–6.73 (Ar-H), 3.69 (t, 2H, N-CH_2), 2.31–2.65 (m, 2H, CH_2), UV–Vis λ_{max} (DMF): 277, and 365 nm.

2.5. X-ray crystallography

The following is a detailed procedure for complex SC-XRD analysis: Crystal data were collected employing Mo Kα (λ = 0.71073 Å, room temperature, 293 K) radiation on a Bruker APEX-II type CCD diffractometer. Bruker SAINT Software was used to perform crystal data reduction [44]. The SADABS software [45] usually rectifies the absorption intensities. The SHELXL-2014 [46,47] software utilization solved and refined the crystal structures. Herein, full-matrix least-squares methods via F^2 have been employed. Anisotropic displacement parameters were applied for non-H atoms. The H atom's positions were fixed based on calculations, which led to a sensitive isotropic. The final CIF file was checked using PLATON [48] and no missing symmetry was confirmed. The crystal structure possesses an A/B-level alert. The alert level in the checkcif has been resolved in the following way: Both alerts are due to bad-quality crystal data. After multiple crystallization attempts, we cannot obtain higher-quality crystal data for this structure.

However, the alerts are present due to poor crystal quality. We are confident that the crystal structure is valid and supported by data from the best crystal. The CCDC number 2,310,357 is associated with the complex. Table 1 summarizes the crystallographic parameters of the complex structure.

2.6. Computational methodology

Multi version computational programs are utilized to elucidate complex properties. These calculations were performed using Gaussian09 RevD.01 and Gauss View 6.0 [49,50]. The methods employed include B3LYP, HF, M06-2x [51–53], and the basis sets used are lanl2dz, add, and def2tzvp. Many quanta chemical calculated parameters describe various chemical properties of the complex [ESI, Section 1.1]. A method for comparing metal complexes' physiological and biological effects concerning proteins is available. Molecular docking (MD) is a commonly used method in molecular biology. MD techniques have been utilized to contrast the biological effectiveness of metal complexes—the investigation utilizing the HEX software. The interactions enhance the biological potency of the interacted compounds [54]. Further, MD calculations compared molecules' biological power in comparison to enzymes. In the HEX 8.0.0 version, the combined files (enzyme and molecule) were analysed [55]. The standard variables are used in MD simulation purposes: correlation type shape only, 3D FFT mode, 0.6-dimensional grid, 180̊-receptor and ligand ranges, 360̊-twist range, and 40̊-distance range. PLIP service [56,57] explains protein–ligand interactions more rigorously. Crystal Explorer 17.5 calculates the HS and 2-dimensional (D) fingerprint plots [58–62] from a structural input file in CIF format. In the context of HS analysis, red, white, and blue colours represent shorter contacts (red), contacts within the van der Waals separation (white), and no close connections (blue).

2.7. Agar Well Diffusion assay

The investigated research compounds were inoculated with standard Gm + ve, Gm-ve, and fungal strains (all mentioned previously) at a temperature of 37.5 °C. The level of bacterial cloudiness was adjusted to match the standard turbidity of 0.5 McFarland units. A standardized inoculum was used to uniformly swab Mueller-Hinton agar plates (Merck, 105437). The dried agar plates with 6 mm wells were spaced approximately 2 cm apart using a sterile cork borer. The bottom of each well was covered with sterilized Mueller-Hinton agar at a temperature of 45.1 °C. The DMSO sample for each microorganism was added to a well and allowed to diffuse for two hours at room temperature. We used streptomycin (+C) for bacterial culture (a + ve control) and DMSO (-C) (a -ve control). In the second and third wells, we used nystatin (+C) as a positive control for fungus. Most microbial plates were incubated face-up in bacterial cultures at 37 °C, 1–2 days preferentially. Notably, the fungal plate grew at room temperature for 5–7 days. It was commonly employed to determine the inhibition zone diameter (IZD) with six replications per plate via microscale. The experimental data were analysed using Origin Pro 8.5′s ANOVA. The common Tukey's standardized test (1 % probability level) separated the mean differences.

Table 1
Crystal data and structure refinement for complex.

Empirical formula	$C_{19}H_{18}Br_2Cl_2CuHgN_2O_4$
Formula weight	833.20
Temperature/K	293.15
Crystal system	monoclinic
Space group	*Cc*
a/Å	8.0018(11)
b/Å	21.538(3)
c/Å	13.4341(18)
α/°	90
β/°	94.444(3)
γ/°	90
Volume/Å^3	2308.4(5)
Z	4
ρ_{calc}g/cm^3	2.397
μ/mm^{-1}	11.287
F(000)	1564.0
Crystal size/mm^3	0.3 × 0.2 × 0.1
Radiation	MoKα (λ = 0.71073)
2Θ range for data collection/°	3.782 to 53.3
Index ranges	$-9 \le h \le 10$, $-26 \le k \le 26$, $-16 \le l \le 16$
Reflections collected	29,810
Independent reflections	4721 [R_{int} = 0.0792, R_{sigma} = 0.0584]
Data/restraints/parameters	4721/110/269
Goodness-of-fit on F^2	1.043
Final R indexes [I>=2σ (I)]	R_1 = 0.0484, wR_2 = 0.1507
Final R indexes [all data]	R_1 = 0.0533, wR_2 = 0.1555
Largest diff. peak/hole / e Å^{-3}	4.72/-4.21
Flack parameter	0.227(19)

2.8. Agar dilution method-MIC determination

The agar dilution method is utilized for the effectiveness of an antimicrobial agent. It involves creating an agar medium with varying agent concentrations through serial 2-fold dilutions. The prescribed microbial inoculum is then introduced on the surface of the agar plate. The MIC endpoint is the lowest concentration of an antimicrobial agent. It completely inhibits growth under suitable incubation conditions—the procedure ideal for testing the susceptibility of both antibacterial and antifungal agents.

3. Results and discussion

3.1. Synthetic perspective

The Schiff base ligand (Salen-type) was synthesized and purified using the previous literature method [3]. A green crystal complex was prepared by grinding solid $CuCl_2{\cdot}2H_2O$ and $HgCl_2$ in methanol-dichloromethane solvent (1:1, v/v) with Schiff base ligand followed by magnetic stirring at 75 °C. The yield of the green needle-type complex is 75 %, and it is structurally characterized by spectroscopy, elemental (CHN), SC-XRD, PXRD, and SEM/EDX approach. The compound remains stable and resistant to air. The coordination chemistry of heteronuclear Cu(II)-Hg(II)-L complexes (L = Schiff base/Salen-type) to X-ray crystal structure and DFT is extensive [1–3,7,15,17]. It is rare to find research that uses DFT-based studies of 6-Bromo-2-hydroxy-3-methoxy benzaldehyde ligand involving Cu(II)-Hg(II)-Salen-type complexes. The studies cover global reactivity, ESP, HOMO-LUMO, NLO, Fukui function, Calculation of interactions energy and energy frameworks, MD, PLIP, and antibacterial and fungal spectrum. The synthetic outline of the ligand and the heteronuclear complex is shown in Scheme 1.

3.2. Characterization

3.2.1. FTIR spectra

The heteronuclear Cu(II)-Hg(II) complex was first characterized by analysing its FTIR spectra (Fig.S1-Fig.S2). The azomethine linkage formation is one of the significant features of the ligand. The same linkage presence in the prepared complex ensures the azomethine nitrogen (N-donor) is coordinated with the metal ions. The FTIR Spectral peak confirmed the presence of the azomethine linkage in both the ligand and the complex. Due to the ligand's azomethine ν(C = N) group formation, a band appears at 1627 cm^{-1}, and the same azomethine linkage shifts to 1640 cm^{-1} for the complex [12,63,64]. Besides, other significant peaks in the complex were identified at 1209 cm^{-1} for C−O, 2950–3370 cm^{-1} for C–H, 600 cm^{-1} for Cu−O, and 789 cm^{-1} for Cu − N [9].

3.2.2. Raman spectra

We also further characterize the complex using a Raman

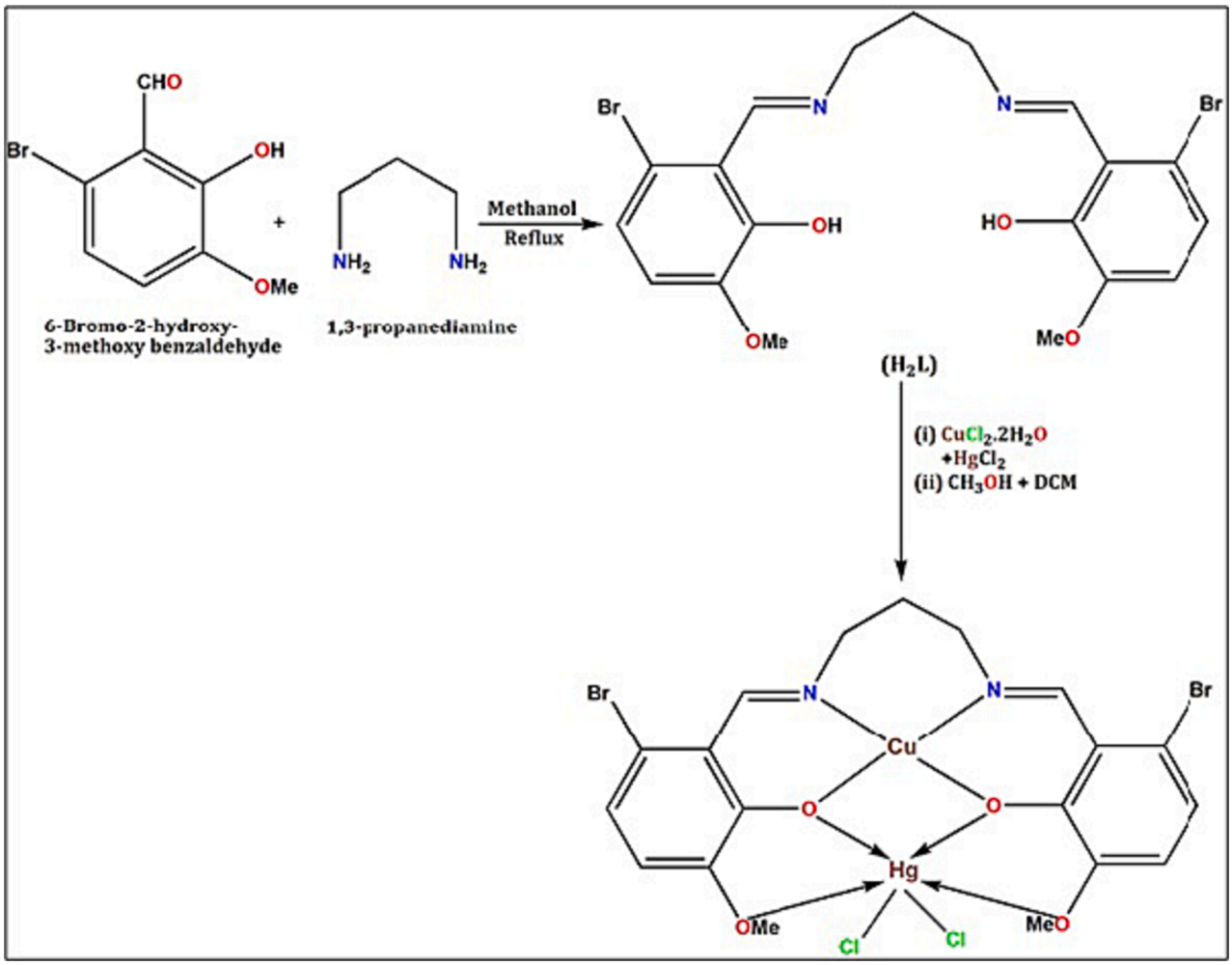

Scheme 1. The synthetic outline of ligand and the complex.

spectroscopic study (Fig.S3). Raman's analysis confirms the presence of azomethine group (C=N) at 1620 cm^{-1} in the complex. The spectral study further identified 1225 cm^{-1} for C–O, 2849–2995 cm^{-1} for C–H, 631 cm^{-1} for Cu–O, and 745 cm^{-1} for Cu–N. Raman spectra serve as crucial tools for structural diagnostics in complex characterization.

3.2.3. UV spectrum

The UV–visible spectra of the synthesized compounds were examined in methanol and dimethyl formamide (Fig.S4-Fig.S5.) The new ligand UV bands are explored at 215 and 243 nm, which correspond to the $\pi \rightarrow \pi^*$ and $n \rightarrow \pi^*$ transitions. The complex exhibits a ligand-based spectrum at 277 and 365 nm (Fig.S4) due to the $L \rightarrow M$ CT transition ($\pi \rightarrow \pi^*/n \rightarrow \pi^*$). UV peak values are identical to the published Cu(II)-Hg (II)-Schiff base complexes [1–3,7,15,17].

3.2.4. NMR study

We characterized the priority basis of the Schiff base ligand using combined ^{1}H and ^{13}C NMR spectroscopy (Fig.S6-Fig.S7), whereas the complex ^{1}H NMR tool was used exclusively (Fig.S8). The peak that appears broadly at δ 13.53 ppm is linked to the phenolic protons (OH) of the ligand. The ligand's significant – CH = N – protons' resonances appear at 8.73–8.68 ppm in the ^{1}H NMR spectra. The resonance peak identified at 3.61–3.78 ppm indicates the presence of protons in the $–OCH_3$ group. The CH_3 proton peaks are observed at 2.08–2.51 ppm. The Salen ligand ^{13}C NMR spectra displayed peaks ranging from 114.78 to 149.49 ppm for Arom-C, 157.56–165.42 ppm for C-OH, and 167.07 ppm for CH = N. In conclusion, the structural frame of the ligand's aromatic and aliphatic components is supported by the ^{13}C NMR spectra. The ligand's O–H proton signal disappears in the complex's ^{1}H NMR spectra, indicating deprotonation and O-atom coordination with Cu(II) metal ions [65,66]. Protons of azomethine (–HC = N-) appear in the complex at 8.27 ppm [67]. The aromatic protons resonate at 6.25–6.73 ppm.

3.2.5. EDX-SEM

The complex was analysed using EDX-SEM microscopy to visualize its elemental composition and morphology [68]. Scanning electron microscopy (SEM) was utilized to determine size-based supramolecular contacts. EDX mapping shows a significant metal composition of Cu and Hg in addition to O and Cl (Fig.S9). The weight % ensures the same. The Cu(II)-complex displays a crystalline ice structure that appears more organized (Fig.S10). The SEM morphology confirms the Cu(II)-Hg(II) reaction in the presence of Schiff base ligands.

3.2.6. Powder X-ray diffraction

We standardized the prepared Cu(II)-Hg(II) complex using the powder x-ray diffraction method. The said method characterizes the complex phase purity and bulk consistency. The bulk products' experimental PXRD patterns match simulated XRD patterns from SCXRD with complex purity and consistency. Complex PXRD patterns were simulated using CCDC Mercury software from SCXRD and CIF files. Fig. S11 displays the PXRD graph of the complex.

4. Crystal structure description

The determination of the X-ray crystal structure reveals that the complex crystallizes in the monoclinic space group *Cc*. The molecular structure of the complex is built from isolated hetero-dinuclear molecules of $[Cu(L)Hg(Cl)_2]$. Important bond lengths/bond angles and the complex perspective view are gathered in Table S1 and Fig. 1, respectively. The Schiff base, Salen-type (H_2L), is a potential N_2O_4 donor compartmental Schiff base having inner N_2O_2 and outer O_4 compartments with copper(II) occupying the inner N_2O_2 cavity and mercury(II) occupying the outer O_4 cavity. Copper(II) is tetracoordinated in the complex, whereas the mercury(II) centre is hexacoordinated. The referenced geometrical environments are comparable to the published heteronuclear Cu(II)-Hg(II) complexes (Table S2). The copper(II) centre, Cu(1), has distorted square planar geometry, where two imine nitrogen atoms, N(1) and N(2), and two phenoxy oxygen atoms, O(2) and O(3), of the deprotonated di-Schiff base constitute the equatorial plane. The Cu–N bond distances (1.953 Å) are comparatively longer than the Cu–O bond distances (1.923 Å). The deviations of the coordinating atoms, O (2), O(3), N(1) and N(2), in the basal plane from the mean plane passing through them are −0.315(14), 0.321(15), 0.272(16) and −0.274(16) Å, respectively, in the complex. The deviation of Cu(1) from the same plane is negligible, being −0.004(2) Å in the complex. Both the trans angles, O (3)–Cu(1)–N(1)and O(2)–Cu(1)–N(2), are found to be 160.9 (7)°. Mercury(II) centre is coordinated by two phenoxy oxygen atoms, O(2) and O (3) in the range 2.53(1)–2.54(1) Å, and two methoxy oxygen atoms, O (1) and O(4), in the significantly longer range 2.67(2)–2.69(2) Å. Chloride anions occupy the two other positions. Both Cl(1) and Cl(2) are attached to mercury(II) at a distance of 2.334(6) and 2.333(6) Å, respectively. The bridging angles, Cu(1)–O(2)–Hg(1) and Cu(1)–O(3)–Hg(1), are 107.5(6)° and 107.0(6)°, respectively. The dihedral angles between the Cu(1), O(2),O(3) and Hg(1),O(2),O(3) planes are 1.21° indicating that the complex core Cu(1),O(2),O(3),Hg(1) is almost planar. Distances between the metal centres [copper(II) and mercury (II)] are 3.607(3) Å. The saturated six-membered chelate ring [Cu(1)–N (1)–C(9)–C(10)–C(11)–N(2)] has an envelope conformation with puckering parameters q = 0.65(2) Å, θ = 115(17)°, and ϕ = 33.4(19)°.

4.1. Supramolecular interactions

Three hydrogen atoms, H(1C), H(11B), H(16), attached to carbon atoms, C(1), C(11), C(16) respectively forms three hydrogen bonds with three symmetry-related (-1 + x,y,z, −1 + x,1-y,-1/2 + z, −1.5 + x,1.5-y,-1/2 + z) chlorine atoms Cl(1). Another hydrogen atom, H(19B), attached to a carbon atom, C(19), forms an intermolecular hydrogen bond with a symmetry-related (-1 + x,y,z,) chlorine atom, Cl(2). Fig. 2 shows the perspective view of the hydrogen bonding interactions. The details of the geometric features of the hydrogen bonding interactions are given in Table 2.

Hydrogen atoms, H(9B) and H(11A) attached to carbon atoms, C(9) and C(11) respectively are involved in inter-molecular C-H•••π interactions with symmetry-related phenyl rings [C(13) − C(14) − C(15) − C(16) − C(17) − C(18)] (x,1-y,-1/2 + z) and [C(2) − C(3) − C(4) − C (5) − C(6) − C(7)] (x,1-y,1/2 + z) respectively to form a dimer (Fig. 3). The details of the geometric features are given in Table 3.

The complex forms a 1D structure (Fig. 4) through type-II halogen bonding interactions formed between bromine atoms [Br(1) and Br(2)] present in the complex. The geometric parameters are X•••X = 3.622 (2), ∠C-X•••X = 140.5(7).

5. DFT profiles

5.1. Hirshfeld surface

The Hirshfeld surface (HS) of the heteronuclear complex has been mapped with the help of d_{norm} (-0.5 to 1.5 Å), shape index (-1.0 to 1.0 Å), and curvedness (-4.0 to 0.4 Å), (Fig. 5, top). The significant contribution (bright red region) on Hirshfeld surface plots is for H…Cl (21.9 %) contacts. Minor contributions from H…Br, H…N and H…O contacts are also spotted. Apart from these, several metal-based contacts are also noticed, i.e., H…Cu, H…Hg etc. (Fig. 5, bottom). 2-D fingerprint plots have been established for these above-mentioned contacts (Fig. 5, bottom). Therefore, combining HSA and 2-D fingerprint plots provides a more comprehensive understanding of the supramolecular interactions in the heteronuclear complex.

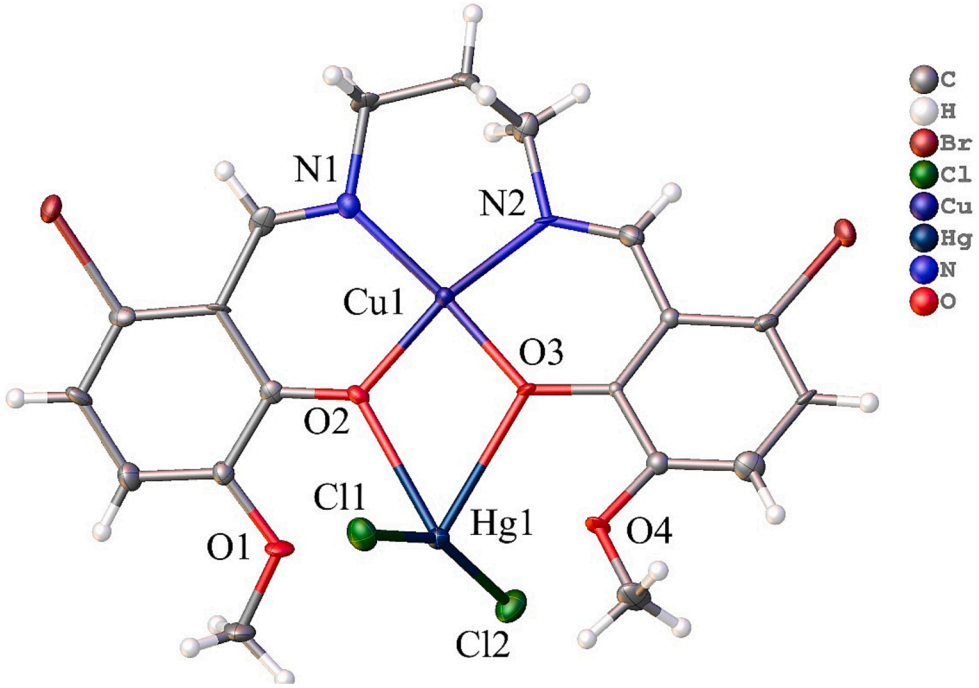

Fig. 1. Complex perspective view with atom numbering scheme.

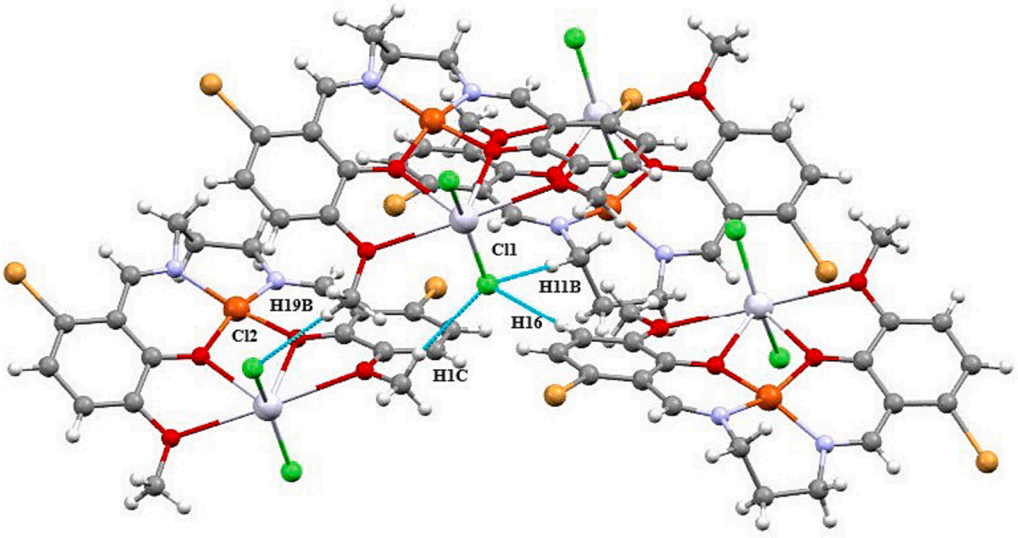

Fig. 2. Perspective view of the H-bonding interactions in the complex with atom numbering scheme.

Table 2
Hydrogen bond distances (Å) and angles (°) of the complex.

D-H•••A	D-H	H•••A	D•••A	∠D-H•••A
C(1)-H(1C)-Cl(1)[a]	0.96	2.72	3.66(2)	167
C(11)-H(11B)-Cl(1)[b]	0.97	2.85	3.81(2)	166
C(16)-H(16)-Cl(1)[c]	0.93	2.83	3.75(2)	170
C(19)-H(19B)-Cl(2)[a]	0.96	2.86	3.82(2)	174

[D = donor; H = hydrogen; A = acceptor. [a] = -1 + x, y,z, [b] = -1 + x,1-y,-1/2 + z [c] = -1.5 + x,1.5-y,-1/2 + z].

5.2. Calculations of interaction energy and energy frameworks

The energy calculation, HF/3-21G, available in Crystal Explorer 17 has been used to calculate the intermolecular interaction energies (IE) (Table 4), where a cluster of molecules is generated by applying crystallographic symmetry operations concerning a selected central molecule within the radius of 3.8 Å by default [69]. The total intermolecular energy (Etot) is the sum of electrostatic (Eele), polarization (Epol), dispersion (Edis), and exchange-repulsion (Erep) energies with scale factors of 1.019, 0.651, 0.901, and 0.811, respectively [70]. The calculated interaction energies (kJ/mol) are: –47.2 (Eele), –26.6 (Epol), –260.8 (Edis), 145.3 (Erep), and –185.2 (Etot). The dispersion energy has a clear dominance over the other interaction energies (Fig. 6). This is because of the presence of halogen atoms with higher electrons/electron clouds. The electrostatic energy is lower due to the absence of classical hydrogen bonds. The energy frameworks represent the intermolecular interaction energies with their magnitude in a pictorial way [71]. Energies between molecular pairs are represented as cylinders joining the centroids of pairs of molecules. The cylinder radius is proportional to the

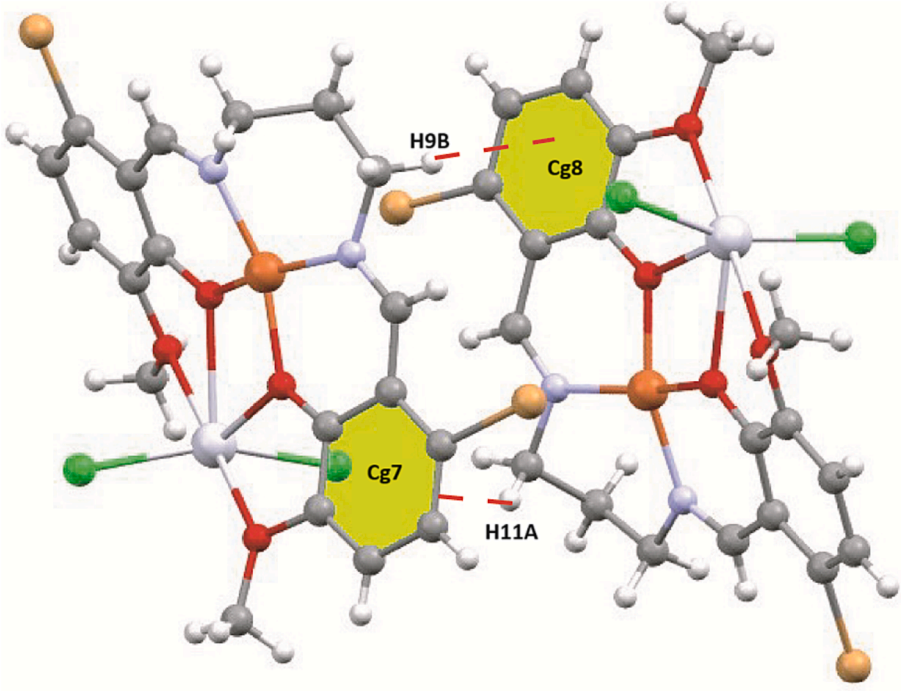

Fig. 3. Perspective view of the hydrogen bonding interactions in the complex with atom numbering scheme.

Table 3
Geometric features (distances in Å and angles in °) of the C-H···π interactions obtained in the complex.

C-H···Cg (Ring)	H···Cg (Å)	C-H···Cg (°)	C···Cg (Å)	Symmetry
C(9)-H(9B)···Cg(8)[a]	2.90	146	3.74(2)	a = x,1-y,-1/2 + z
C(11)-H(11A)···Cg (7)[b]	2.89	129	3.58(2)	b = x,1-y,1/2 + z

[Cg(7) = Centre of gravity of the ring [C(2) – C(3) – C(4) – C(5) – C(6) – C(7)]; Cg(8) = Centre of gravity of the ring [C(13) – C(14) – C(15) – C(16) – C(17) – C(18)].

relative strength of the corresponding interaction energy [72]. Energy frameworks are constructed for E_{ele} (red cylinders), E_{dis} (green cylinders), and E_{tot} (blue cylinders) (Fig. 6).

5.3. Frontier molecular orbital

The realm of theoretical calculations offers a vast playground for exploring and dissecting the myriad properties exhibited by molecules. The Gaussian package program is at the forefront of this scientific endeavour, a powerful computational tool capable of evaluating many quanta chemical parameters. Among these parameters, E_{HOMO} and E_{LUMO} (HOMO-LUMO stands for usual meaning) emerge as paramount, guiding our understanding of molecular activities. E_{HOMO} gauges a molecule's propensity to donate electrons [73], while E_{LUMO} provides insights into its ability to accept electrons [74]. These two parameters, often considered the yin and yang of molecular reactivity, form the cornerstone for unravelling the enigma of molecular behaviour. Beyond E_{HOMO} and $E_{LUMO,}$ another indispensable parameter in our theoretical chemistry is the ΔE energy gap value. A large energy gap indicates thermodynamic stability; a small means reactivity and polarity [75]. In our complex, we studied different DFT levels for the Frontier molecular orbital (FMO) analysis (Table 5, Fig. 7c). According to such analysis, it is reliable that the complex is thermodynamically stable for the HF/3-21 g LEVEL, while the complex is reactive and polar for B3LYP/6-31 g.

5.4. Global reactivity parameters

Global reactivity descriptors are generated using the HOMO and LUMO orbital energies [76]. The synthesized complex's stability, selectivity, hardness/softness, and reactivity primarily depend on global reactivity factors [77,78]. Furthermore, electronegativity serves as a critical factor in a molecule's activity level, with its numerical value indicating the molecule's inclination toward chemical engagement. A lower value correlates with greater reactivity [75]. Tabulated reactivity parameters and their corresponding computed values are listed in Table 5. We obtained a lower electronegativity value based on our DFT studies using B3LYP/6-31 g Level. Based on the calculations, we can conclude that the complex is reactive.

5.5. ESP profile

In ESP (electrostatic potential) investigation, the colour code indicates the areas within a molecule prone to E^+ and Nu^- reactions. Uniformly, the ESP increases as follows: red < orange < yellow < green < blue [79]. Fig. 7(a-c) shows the optimized structure (a), ESP (b), and HOMO-LUMO (c) representations of the metal complex molecule. The ESP representation shows the molecule's electron density. Regions of the highest electron density in the metal complex molecule are shown in red. In contrast, the blue areas have the lowest electron density [80]. Generally, the areas with high electron density donate electrons, and those with low electron density accept them. The ESP study of the complex reveals that ligand O-donor atoms exhibit a red hue, having the highest electron density. Further, N-donor atoms of the ligand predominantly display a deep blue area, indicating minimum electron density. The light blue regions explore the metal centre. Red means our complex's optimal electrophilic attack site, and blue is best for nucleophilic attack. In Fig. 7, the optimized structure of the complex (7a) is given, and then the HOMO and LUMO view of the molecule from this optimized structure is provided (7c). In these pictures, it is seen which atoms have HOMO and LUMO orbital characters in the complex. Finally, the complex ESP view is given in (7b), in which the electron density of the complex is explored. The appearance of the red-coloured regions of the molecule's HOMO figure and ESP shows that, depending on the electron density in the molecule, these are regions with high electron density, which allows the electrophile to attack these regions. On the other hand, the blue areas in the LUMO Figure and ESP of the molecule allow nucleophile attacks. We analysed the optimized structure, HOMO-LUMO, and ESP profiles of the complex to identify electrophilic (E^+) and nucleophilic (Nu^-) attacking zones which are meaningless without the ESP approach.

5.6. Fukui function

Fukui indices provide valuable information about a molecule's ability to donate or accept electrons. It also includes helpful information regarding marked atoms in a compound most susceptible to undergo E^+/Nu^- reactions. The atomic or condensed Fukui functions within the atomic domain 'j' can be established using the following formulas (ESI, Section 1.2). In the provided equations, the parameters $f_j^-(r)$ and $f_j^+(r)$ indicate the reactivity of atoms within the reference molecule towards E^+/Nu^-, or free radical-type reactions. These equations utilize the variable qj, Neutral (N), anionic (N + 1), or cationic (N–1) chemical species, each having a mathematical atomic charge in the jth nuclear region. The value is determined through the Mulliken population or charge derived from electrostatic. The binary descriptor Δf(r) represents the difference between Nu^- and E^+ Fukui functions and can be calculated using equations [81,82]. For the Δf(r) > 0 or < 0, condition is suitable for Nu^-/E^+ reactions. Therefore, Δf(r) provides a particular site E^+/Nu^--attacking reactions. Henceforth, atoms with a tendency to Nu- attack are assigned a + ve value, while those with movement to E + attack are given a -ve

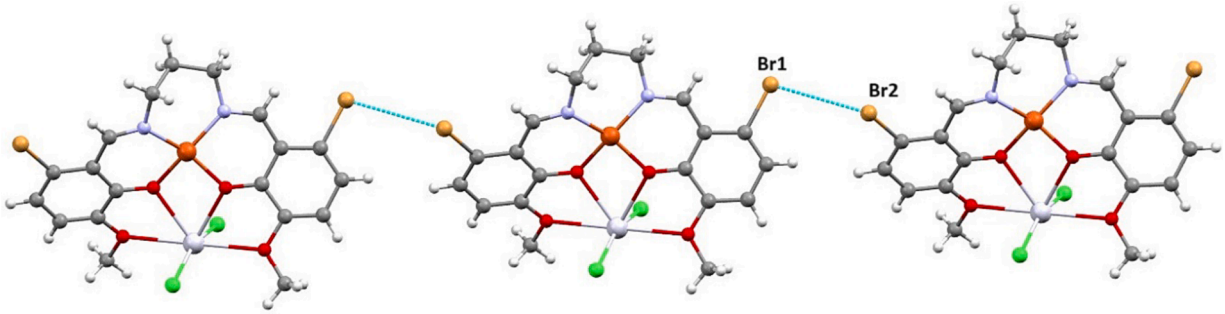

Fig. 4. Perspective view of the halogen bonding interactions in the complex resulting in a 1D structure.

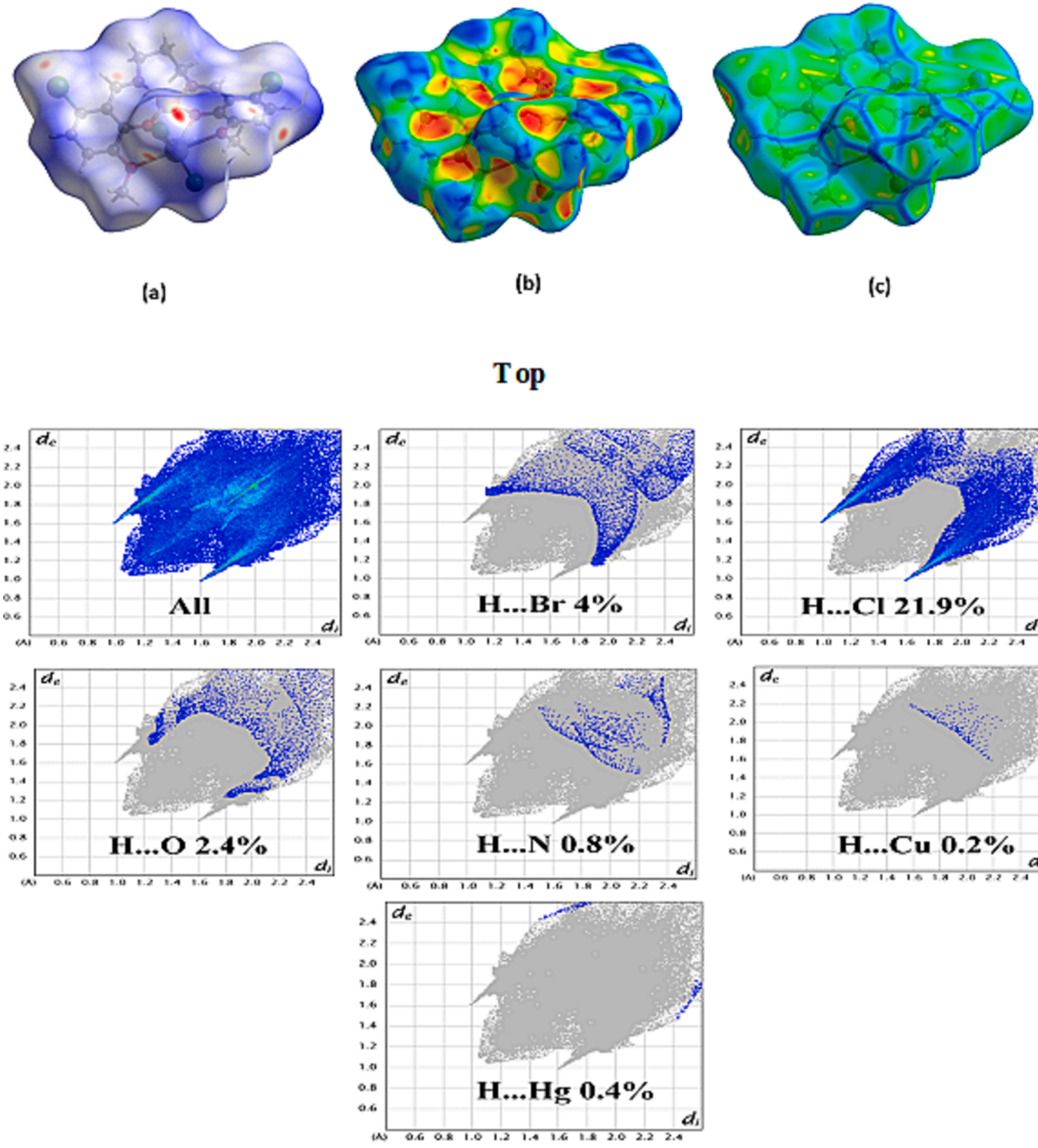

Fig. 5. HS mapped with d_{norm} (a), shape index (b), and curvedness (c), (top), and 2-D fingerprint plots (bottom) in the complex.

value [83]. Concerning our complex, Nu^- attack is associated with 4 Cu (highest + ve, +0.58), while E^+ attack for 10 N and 11 N (lowest -ve −0.20 atoms) (Table S3, Fig.S12). The complex reactivity of E+/Nu- attacking reactions depends on the atoms in the surrounding environment of the studied compounds. The numerical values obtained from the Fukui function agreed well with the results of the electrostatic potential (ESP) [75].

5.7. NLO activities

Optical memory devices, signal processing, optical switches, and communication technology heavily rely on NLO-studied com-

Table 4
Different interaction energies of the molecular pairs (kJ/mol).

N	Symmetry operation	R	Electron Density	E_ele	E_pol	E_dis	E_rep	E_tot
1	x, y, z	15.09	HF/3-21G	−3.3	−0.4	−11.0	13.8	−2.3
1	x, -y, z + 1/2	10.14	HF/3-21G	3.2	−4.5	−52.3	26.0	−25.7
0	–	9.82	HF/3-21G	1.4	−0.1	−1.2	0.0	0.2
0	x, y, z	8.00	HF/3-21G	1.8	−1.5	−9.5	0.4	−7.4
0	x + 1/2, y + 1/2, z	11.49	HF/3-21G	0.0	−1.3	0.0	0.0	−0.8
1	x, -y, z + 1/2	6.87	HF/3-21G	−44.4	−12.7	−91.1	64.0	−83.8
0	–	3.46	HF/3-21G	1.8	−1.5	−9.5	0.4	−7.4
1	–	9.34	HF/3-21G	0.3	−0.0	−1.1	0.0	−0.7
0	–	8.07	HF/3-21G	3.2	−4.5	−52.3	26.0	−25.7
0	–	8.30	HF/3-21G	0.1	−0.0	−0.2	−0.0	−0.1
0	–	8.53	HF/3-21G	−1.5	−0.1	−0.8	0.0	−2.3
1	x + 1/2, -y + 1/2, z + 1/2	12.01	HF/3-21G	−10.4	−2.3	−17.1	6.3	−22.4
0	x + 1/2, y + 1/2, z	11.49	HF/3-21G	0.6	−1.5	−14.7	8.4	−6.8

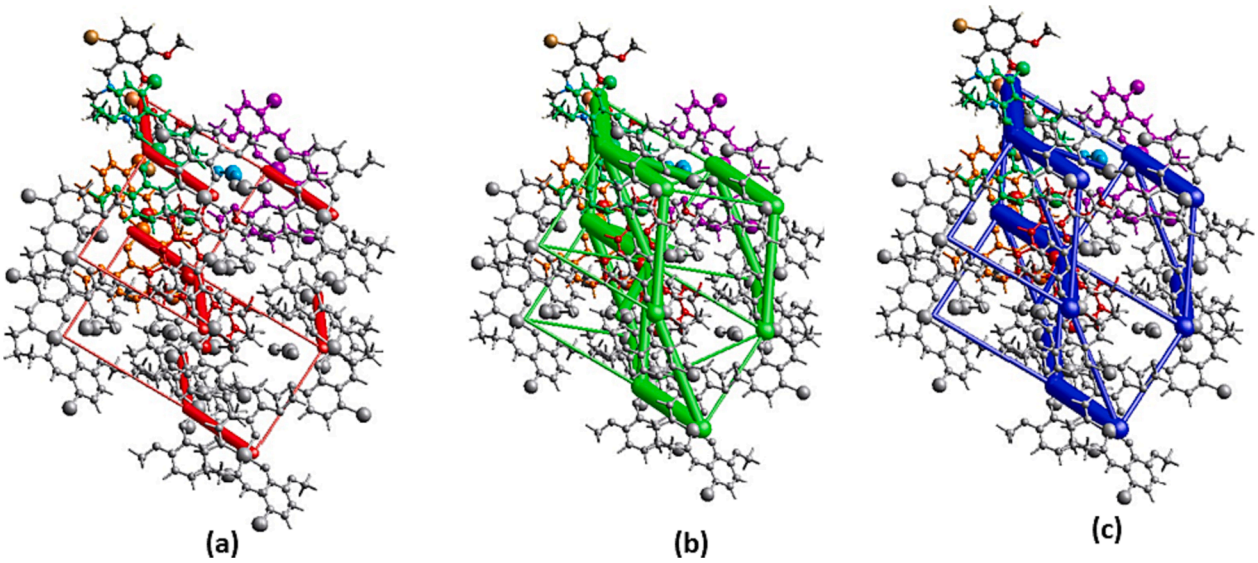

Fig. 6. Perspective views of electrostatic energy (a), dispersion energy (b), and total energy diagrams (c) constructed from the energy framework for a cluster of molecules in the complex (The cylindrical radius is proportional to the relative strength of the corresponding energies, Scale factor used is 100 with cut-off values of 10 kJ/mol).

Table 5
The calculated quantum chemical parameters.

E_{HOMO}	E_{LUMO}	I	A	ΔE	η	μ	χ	Pi	ω	ε	dipole	Energy
B3LYP/3-21g LEVEL												
−6.0728	−2.5663	6.0728	2.5663	3.5065	1.7532	0.5704	4.3196	−4.3196	5.3212	0.1879	9.874	−39187.097
B3LYP/6-31g LEVEL												
−5.8987	−2.4839	5.8987	2.4839	3.4148	1.7074	0.5857	4.1913	−4.1913	5.1443	0.1944	6.590	−66476.875
B3LYP/ 6-31++g LEVEL**												
−5.7747	−2.2395	5.7747	2.2395	3.5352	1.7676	0.5657	4.0071	−4.0071	4.5420	0.2202	4.551	−245134.784
HF/3-21g LEVEL												
−8.4914	0.8515	8.4914	−0.8515	9.3428	4.6714	0.2141	3.8200	−3.8200	1.5619	0.6403	10.917	−38900.083
HF/6-31 g LEVEL												
−8.4163	0.5965	8.4163	−0.5965	9.0128	4.5064	0.2219	3.9099	−3.9099	1.6962	0.5896	9.681	−66172.648
HF/ 6-31++g LEVEL**												
−7.9757	1.4400	7.9757	−1.4400	9.4158	4.7079	0.2124	3.2678	−3.2678	1.1341	0.8817	5.933	−244738.481
M062X/3-21g LEVEL												
−7.3194	−1.5462	7.3194	1.5462	5.7732	2.8866	0.3464	4.4328	−4.4328	3.4036	0.2938	7.465	−39168.951
M062X/6-31g LEVEL												
−7.2965	−1.6811	7.2965	1.6811	5.6154	2.8077	0.3562	4.4888	−4.4888	3.5883	0.2787	7.992	−66457.973
M062X/ 6-31++g LEVEL**												
−7.0769	−1.3837	7.0769	1.3837	5.6932	2.8466	0.3513	4.2303	−4.2303	3.1433	0.3181	5.3561	−245115.215

pounds—the electrical properties of the synthesized complex cause the reaction of light. It is associated to the nonlinear hyperpolarizabilities (β_{tot}) and linear polarizability (α_0) (Table 6). Our analysis of molecules (Fig.S12) involves comparing their dipole moments, which provides information about the direction of charge distribution within them. The dipole moment has a value of 0.4645 a.u to −1.1441 a.u. The ESI parameters (ESI, Section 1.3) can be used to calculate the NLO functions. Compounds' (α_0) and (β_{tot}) numerical values were vividly evaluated.

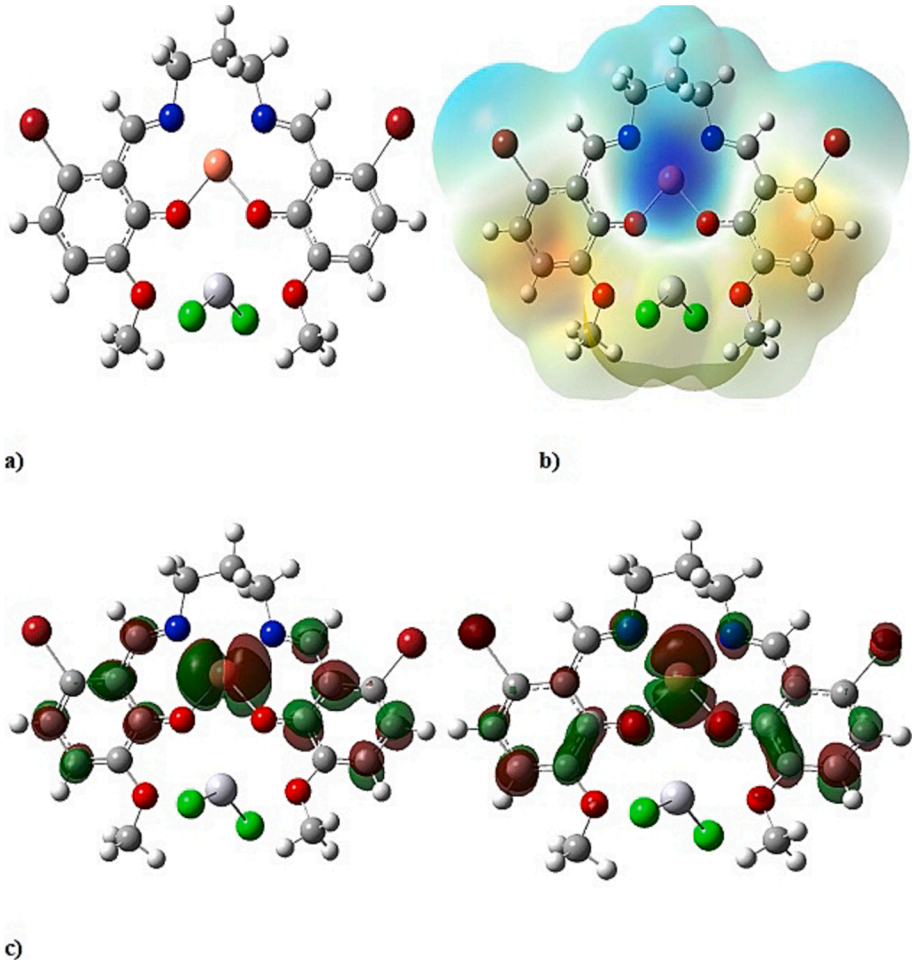

Fig. 7. Representations of Optimize structure (a), ESP (b), and HOMO-LUMO (c) of the complex.

Table 6
Complex computed NLO parameters.

	a.u.	esu		a.u.	esu
α_{xx}	249.2635	$3.689\ 10^{-23}$	β_{xxx}	−207.371	$-1.792\ 10^{-27}$
α_{xy}	−14.3444	$-2.123\ 10^{-24}$	β_{yyy}	81.508	$7.043\ 10^{-28}$
α_{yy}	197.8082	$2.927\ 10^{-23}$	β_{zzz}	−64.099	$-5.539\ 10^{-28}$
α_{xz}	3.4511	$5.107\ 10^{-25}$	β_{xyy}	99.467	$8.595\ 10^{-28}$
α_{yz}	2.9071	$4.302\ 10^{-25}$	β_{xxy}	6.161	$5.325\ 10^{-29}$
α_{zz}	114.1193	$1.688\ 10^{-23}$	β_{xxz}	0.445	$3.849\ 10^{-30}$
Δ_{α}	144.2424	$2.134\ 10^{-23}$	β_{xzz}	7.898	$6.825\ 10^{-29}$
μ_x	0.4645	$6.874\ 10^{-26}$	β_{yzz}	−3.937	$-3.402\ 10^{-29}$
μ_y	−1.1441	$-1.693\ 10^{-25}$	β_{yyz}	2.030	$1.755\ 10^{-29}$
μ_z	−0.1377	$-2.037\ 10^{-26}$	β_{total}	144.255	$1.247\ 10^{-29}$
μ_g	1.2425				

When converting these computed standard data into electrostatic units (esu), they are multiplied by constant values based on the atomic unit (a.u.) As the standard important parameters are increased, so are the compound NLO activities. The maximum contribution of the x-axis polarizability tensor affects the numerical overall linear polarizability (α_0). The maximum polarizability value for the complex is 249.2635 a.u. Table 6 shows the in detail computed characteristics of the metal complex using the very popular basis set HF/6-31++g**.

5.8. MD and PLIP profiles

The use of Gaussian software for molecular calculations may not provide a complete understanding of the biological activities of molecules. Therefore, additional molecular docking (MD) calculations were conducted. The activity of metal–ligand complexes against proteins depends on their chemical interactions. It is widely recognized that as these chemical interactions become more prominent, the activities of the molecules tend to increase. These interactions encompass a variety of chemical forces, including H-bonds, polar/hydrophobic interactions, π-π stacking, and X-bonding (X = Halogen) [84–86]. The augmentation of these interactions often leads to the inhibition of proteins. The pictures of the interactions that occur because of the molecular docking calculations are given in Fig.S13(a-c). Further interactions between the metal complex and proteins were examined via PLIP investigation. The numerical values of the interactions are listed in Tables 7-9. As a result of the PLIP analysis performed because of the calculations, the exchange of the metal complex with various bacteria was examined. Fig. 8a shows that the metal complex makes Hydrophobic Interactions with the Staphylococcus aureus proteins that are VAL, ASN, and LYS at five

Table 7
Hydrophobic Interactions of protein and metal complex.

Index	Residue	AA	Distance	Ligand atom	Protein atom
Staphylococcus aureus protein with molecule					
1	45B	VAL	2.20	11,417	2979
2	58B	VAL	3.36	11,425	3098
3	204A	VAL	2.97	11,417	1736
4	205A	ASN	3.87	11,427	1742
5	266D	LYS	2.98	11,437	10,713
Escherica coli protein with molecule					
1	664A	PHE	3.43	9374	5893
2	664A	PHE	3.73	9382	5891

Table 8
Hydrogen Bonds of protein and metal complex.

Index	Residue	AA	Distance H-A	Distance D-A	Donor angel	Protein donor?	Side chain	Donor Atom	Acceptor Atom
Staphylococcus aureus protein with molecule									
1	205A	ASN	2.35	3.31	160.95	√	√	1745 [Nam]	11,424 [O2]
2	270D	GLN	3.23	3.82	119.03	√	√	10,759 [Nam]	11,421 [O2]
Escherichia coli protein with molecule									
1	652A	THR	3.02	3.76	136.02	√	√	5774 [O3]	9367 [O2]

Table 9
π-cation of protein and metal complex.

Index	Residue	AA	Distance	Offset	Protein charged	Ligand group	Ligands Atoms
Escherichia coli protein with molecule							
1	653A	ARG	4.83	1.95	√	Aromatic	9372, 9387, 9392, 9398, 9400, 9408

different points. On the other hand, Fig. 8b shows that the metal complex makes Hydrophobic Interactions with the Escherichia coli protein that is PHE at 2 different points. In addition, it is seen that the metal complex makes hydrogen bonds with the Staphylococcus aureus protein at two other points, ASN and GLN. At the same time, it is seen that the metal complex interacts with the Escherichia coli protein at that THR at 1 point. When the interactions of molecules with bacteria are examined because of molecular docking calculations, it is seen that the molecule interacts with Staphylococcus aureus and Escherichia coli proteins. Still, there is no interaction between the molecule and the Pseudomonas aeruginosa protein. PLIP supports this situation.

6. Antibacterial and fungal spectrum

The research samples' antimicrobial effects were conducted in favour of two Gm + ve and two Gm-ve bacterial strains and a fungal strain, (Fig.S14) and the procedure is given above—Tables 10 and 11 show mean zone diameter and MIC values. From the mechanistic perspective, the antimicrobial results were compared among the Ligand (**L**), complex (**C1**), Cu-salt ($CuCl_2$), and $HgCl_2$. Results indicate activity against selected microorganisms. In the case of synthesized compounds, action shows favour S. aureus in the order Ligand (10.8 ± 0.2) < Cu-salt (12.3 ± 0.1) < complex (12.6 ± 0.3) < $HgCl_2$ (13.1 ± 0.2), here Ligand shows lower activity, but Cu-salt, complex, and $HgCl_2$ moderate to high activity. Metal complexes show higher activity than ligands due to chelation observed in this case, but unusually, metal salt $HgCl_2$ shows increased activity. B. subtilis activity against selected compounds is of the order Ligand (11.3 ± 0.2) < $HgCl_2$ (12.3 ± 0.3) < Cu-salt (13.2 ± 0.3) < complex (13.8 ± 0.1). In this case, the complex shows higher activity than metal salts, and ligand values vary close to commonly used standard antimicrobial drugs. For E. coli, $HgCl_2$ (11.6 ± 0.3) < Ligand (13.1 ± 0.2) < Cu-salt (15.3 ± 0.3) < complex (25.3 ± 0.2) is the order of activity, in this case complex shows very high activity and its value is higher than standard reference drug. It can be suggested as an alternative to a reference drug. The mechanism behind copper's antimicrobial activity needs to be better comprehended. One hypothetical reason is that it generates hydroxyl radicals [87,88]. When copper is in contact with water, it releases metal ions, such as Cu(I) and Cu(II). Through polarization of the target molecule, ions facilitate hydrolysis followed by nucleophilic attack of the hydroxyl radical. Cu(II) ions can attack bacterial cell membranes, nucleic acids, and proteins, altering their structure and function and ultimately causing cell death [89]. Cu(II) ions selectively bind to the sulfhydryl groups of respiratory enzymes inside a bacterial cell. Under this situation, the bacterial cell membrane attacks essential proteins. The condition is particularly evident in Escherichia coli [87–90]. Therefore, with their antibacterial activity, Cu-based compounds may help treat antibiotic-resistant strains of bacteria such as Escherichia coli. In P. aeruginosa, the order of reactivity is 11.3 ± 0.1 < 12.3 ± 0.1 < 12.8 ± 0.2 < 14.2 ± 0.3, all the compounds show moderate to high activity. The outer membrane of Gm-ve bacteria is highly impermeable and covers their peptidoglycan layer Gm + ve bacteria have a -ve charged polysaccharide, tachyonic acid, in their outer cell wall, facilitating the + ve charged ions' entry into the cell. The high antibacterial activity of the complexes against Gm + ve strains can be attributed to this factor [91]. In the case of C. albicans, antifungal activity is of the order $HgCl_2$ (40.0 ± 0.4) > Cu-salt (32.5 ± 0.4) > Ligand (14.9 ± 0.3), and complex does not show any activity. Also, in the case of A. niger, $HgCl_2$ (52.5 ± 0.1) and Cu–salt (14.4 ± 0.4), and complex are inactive against A. niger. Usually complex, it shows notably higher antifungal activity. But here, metal salts show very high activity against selected microbes. According to significant Overtone's concept, delocalization reduces the lipophobic character of the compound, promoting penetration into bacterial membranes and blocking metal binding sites of microorganism enzymes. H-bond formation between

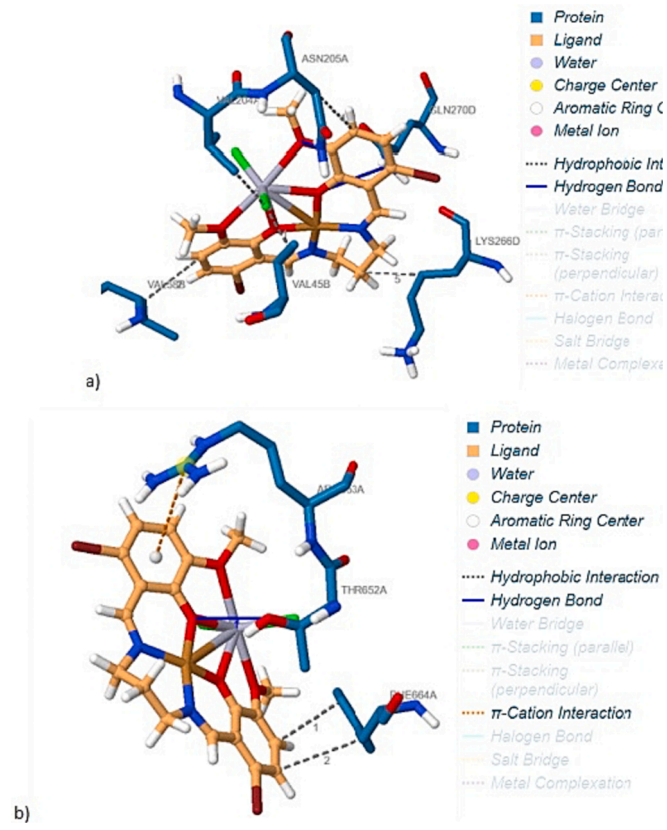

Fig. 8. (a) plip interaction of complex with the staphylococcus aureus protein, and (b) with the Escherichia coli protein.

Table 10
Mean zone diameter.

	Mean zone diameter (mm)a					
	S. aureus	***B. subtilis***	***P. aeruginosa***	***E. coli***	***C. albicans***	***A. niger***
$HgCl_2$	13.1 ± 0.2	12.3 ± 0.3	11.3 ± 0.1	11.6 ± 0.3	40.0 ± 0.4	52.5 ± 0.1
Cu-salt	12.3 ± 0.1	13.2 ± 0.3	14.2 ± 0.3	15.3 ± 0.3	32.5 ± 0.4	14.4 ± 0.4
Ligand	10.8 ± 0.2	11.3 ± 0.2	12.3 ± 0.1	13.1 ± 0.2	14.9 ± 0.3	–
Complex	12.6 ± 0.3	13.8 ± 0.1	12.8 ± 0.2	25.3 ± 0.2	–	–
Chloramphenicol	15.0 ± 0.4	14.0 ± 0.4	15.0 ± 0.4	16.0 ± 0.1	–	–
Nystatin	–			–	19.0 ± 0.1	19.2 ± 0.2
DMSO	–			–	–	

Each value represents a mean ± standard deviation (SD) of three replications.
[a] the zone diameters have been calculated in mm. –: not detected inhibition.

Table 11
MIC values of the compounds.

	MIC (μg/mL)					
	S. aureus	***B. subtilis***	***P. aeruginosa***	***E. coli***	***C. albicans***	***A. niger***
$HgCl_2$	6.25 ± 0.2	6.25 ± 0.1	25 ± 0.3	12.5 ± 0.2	3.125 ± 0.3	3.125 ± 0.1
Cu-salt	12.5 ± 0.2	3.125 ± 0.1	6.25 ± 0.2	6.25 ± 0.3	6.25 ± 0.2	12.5 ± 0.4
Ligand	25 ± 0.4	12.5 ± 0.3	12.5 ± 0.4	12.5 ± 0.4	25 ± 0.5	–
Complex	12.5 ± 0.4	3.125 ± 0.1	12.5 ± 0.4	3.125 ± 0.1	–	–
Chloramphenicol	3.125 ± 0.3	3.125 ± 0.2	3.125 ± 0.2	3.125 ± 0.1		
Nystatin	–	–			6.25 ± 0.2	6.25 ± 0.2
DMSO	–	–	–	–	–	–

–: not detected inhibition.

metal salts and cell constituents can disrupt normal cell processes, leading to bacterial cell death. Various factors affect compound activity, including the nature of the M(II) ion, complex coordinating sites/geometry, hydrophilicity, and lipophilicity. The metal ions have a strong bonding capacity but are not readily available for activity. However, the Schiff base ligand and its complexes exhibit no activity due to their low lipid solubility [92].

7. Conclusion

In brief, we synthesized and structurally characterized one new heteronuclear Cu(II)-Hg(II)-Salen-type complex. SCXRD reveals that the complex crystallized space group Cc. X-ray diffraction confirms tetra and hexacoordinated arrangement around Cu(II) and Hg(II) ions. The crystal structure displays unique supramolecular interactions, including intermolecular C-H•••π H-bonding and X-bonding (X = halogen, Br). The complex was subjected to DFT calculations based on the Gaussian software package at the B3LYP, HF, and M062x levels. In the complex, HOMO-LUMO, ESP, and global reactivity support reactivity in a new portfolio. The complex exhibited promising nonlinear optical activity (NLO), with wide-ranging technological applications. The Fukui function calculation can identify regions susceptible to Nu^- (nucleophilic) and E^+ (electrophilic) attacks. The molecular docking and PLIP investigation indicated possible antimicrobial activity against bacterial and fungal strains. Experimental findings have confirmed the antibacterial and fungal properties of the complex, which were found to be as effective as standard drugs. The research article showcases how complex can be used rapidly as medicinal and antimicrobial agents. Finally, the report analysed by MD/PLIP has been of great interest to researchers of the molecular dynamics community.

Acknowledgments and Funding

This research has yet to receive specific funding from any funding agency in the public, commercial, or non-profit sectors. All authors thank the Central Laboratory of Tamralipta Mahavidyalaya, Purba Medinipur, Tamluk-721636, West Bengal, India, funded by the DST-FIST project (Level-0) under the Department of Science and Technology (DST), Govt. from India. All authors carefully read and approved the final version before submission.

Author contributions

Dr. Dhrubajyoti Majumdar was the project administrator and conceived the whole research idea, performed data curation, conceptualization, methodology, research investigation, software visualization, interpreted the data, contributed reagents, materials, analysis tools or data, writing complete review, editing, and wrote the paper. **Dr. Sourav Roy** Software utilization, visualization, various graphics preparation, analysis tools or data, and wrote the paper. **Dr. Jessica Elizabeth Philip** performed the experiments, analysed, and interpreted the tools or data. **Dr. Burak Tüzün** performed DFT experiments, analysis tools or data and wrote the article. **Suman Hazra** Software utilization, visualization, various graphics preparation, analysis tools or data. Before submission, all manuscript authors thoroughly read and endorsed the final version.

Declarations

Resolution of A/B-level alert in the checkcif report

The crystal structure possesses an A/B-level alert, as the checkcif report supports. The alert levels in the checkcif information have been resolved in the following manner: The alert is due to insufficient quality data. We crystallized several times to obtain better-quality crystal data for this structure; however, the residual density value is high due to twinning, disorder, poor crystal quality, etc. We are confident that the crystal structural characterization and the data from the best crystal are valid. We have included the resolution in the updated manuscript under the X-ray crystallography section.

CRediT authorship contribution statement

Dhrubajyoti Majumdar: Writing – review & editing, Writing – original draft, Validation, Supervision, Software, Resources, Project administration, Methodology, Investigation, Funding acquisition, Formal analysis, Data curation, Conceptualization. **Sourav Roy:** Visualization, Validation, Software, Formal analysis, Data curation. **Jessica Elizabeth Philip:** . **Burak Tüzün:** Visualization, Validation, Software, Formal analysis, Data curation. **Suman Hazra:** Visualization, Validation, Software, Formal analysis.

Declaration of competing interest

The authors declare that they have no known competing financial interests or personal relationships that could have appeared to influence the work reported in this paper.

Data availability

The data that has been used is confidential.

Appendix A. Supplementary material

Supplementary data to this article can be found online at https://doi.org/10.1016/j.inoche.2023.111933.

References

[1] L.T. Yıldırım, R. Kurtaran, H. Namli, A.D. Azaz, O. Atakol, Polyhedron 26 (2007) 4187–4194.
[2] L.K. Das, C.J. Gómez-García, M.G.B. Drew, A. Ghosh, Polyhedron 87 (2015) 311–320.
[3] D.J. Majumdar, B. Tüzün, T.K. Pal, R.V. Saini, K. Bankura, D. Mishra, Polyhedron 210 (2021), 115504.
[4] D.J. Majumdar, D. Das, S. Nag, M. Bhattacharyya, D.K. Singh, D. Parai, K. Bankura, D. Mishra, J. Mol. Struct. 1222 (2020), 128951.
[5] D.J. Majumdar, B. Tüzün, T.K. Pal, S. Das, Kalipada Bankura, J. Inorg. Organomet. Polym. 32 (2022) 1159–1176.
[6] D.J. Majumdar, A. Frontera, R.M. Gomila, S. Das, K.P. Bankura, RSC Adv. 12 (2022) 6352–6363.
[7] M. Dolai, T. Mistri, A. Panja, M. Ali, Inorg. Chim. Acta. 399 (2013) 95–104.
[8] L.-L. Gan, X. Li, M.-X. Du, Y.-J. Yan, Y. Zhang, W.-K. Dong, Y.-J. Ding, J. Mol. Struct. 1299 (2024), 137199.
[9] X.-X. Li, C.-Y. Ma, M.-X. Du, W.-K. Dong, Y.-J. Ding, J. Mol. Struct. 1299 (2024), 137188.
[10] C.-Y. Ma, X.-X. Li, M.-X. Du, W.-K. Dong, Y.-J. Ding, J. Mol. Struct. 1298 (2024), 137071.
[11] Y-T. La, M-X. Du, L-L Gan, Y. Zhang, Y-X. Sun, W-K. Dong, Spectrochim. Acta. Part A. 305 (2024) 123481.
[12] K. Sarmah, G. Pandit, A.B. Das, B. Sarma, S. Pratihar, Cryst. Growth Des. 17 (1) (2017) 368–380.
[13] C. Santini, M. Pellei, V. Gandin, M. Porchia, F. Tisato, C. Marzano, Chem. Rev. 114 (2014) 815–862.
[14] K. Das, A. Datta, C. Sinha, J.H. Huang, E. Garribba, C.S. Hsiao, C.L. Hsu, Chemistry Open 1 (2012) 80–89.
[15] I.F. Chavez-Urias, L.E. Lopez-Gonzalez, D.F. Plascencia-Martinez, J.J. Garcia, M. Flores-Alamo, R. Sugich-Miranda, F. Medrano, L.A. Picos-Corrales, E.F. Karla-Alejandra Lopez-Gastelum, F.-A. Velazquez-Contreras, ACS Omega 8 (2023) 24601–24614.
[16] P.H.O. Santiago, C.M. Aiube, J.L. de Macedo, C.C. Gatto, Mol. Catal. 496 (2020), 111177.
[17] T.L. Yusuf, S.D. Oladipo, S. Zamisa, H.M. Kumalo, I.A. Lawal, M.M. Lawal, N. Mabuba, ACS Omega 6 (2021) 13704–13718.
[18] Y.-W. Dong, R.-Q. Fan, P. Wang, L.-G. Wei, X.-M. Wang, S. Gao, H.-J. Zhang, Y.-L. Yang, Y.-L. Wang, Inorg. Chem. 54 (16) (2015) 7742–7752.
[19] F.A. Cotton, G. Wilkinson, Anorganische Chemie, Interscience Publishers, Weinheim, 1967.
[20] N.L. Holy, N.C. Baezinger, R.M. Flyn, D.C. Swendon, J. Am. Chem. Soc. 98 (1976) 7823.
[21] I. Ercan, F. Ercan, C. Aricib, O. Atakol, Acta Cryst. C 58 (2002) m137–m138.
[22] A. Bulut, O.Z. Yesilel, N. Dege, H. Icbudak, H. Olmez, O. Buyukgungor, Acta Cryst. C 59 (2003) o727–o729.
[23] S. Genç, N. Dege, A. Çetin, A. Cansız, M. Şekerci, M. Dinçer, Acta Crystallographica Section E: Structure Reports Online 60 (9) (2004) o1580–o1582.
[24] N. Dege, H. Içbudak, E. Adıyaman, Acta Cryst. C 62 (2006) m401–m403.
[25] M. Arıcı, O.Z. Yeşilel, E. Acar, N. Dege, Polyhedron 127 (2017) 293–301.
[26] S. Dhibar, S. Pal, K. Karmakar, Sk A. Hafiz, S. Bhattacharjee, A. Roy, S. K. Mehebub Rahaman, S. J. Ray, S. Dam, B. Saha, RSC Adv. 13 (2023) 32842.
[27] D.J. Majumdar, A. Dubey, A. Tufail, D. Sutradhar, S. Roy, Heliyon (2023) e16057.
[28] R. Hussain, S.L. Rubab, A. Maryam, T. Ashraf, M. Arshad, K. Lal, S.H. Sumrra, S. Ashraf, B. Ali, ACS Omega 8 (45) (2023) 42598–42609.
[29] D. Avcı, S. Altürk, F. Sönmez, Ö. Tamer, A. Başoğlu, Y. Atalay, B.Z. Kurt, D. Öztürk, N. Dege, Appl. Organomet. Chem. 33 (3) (2019) e4725.
[30] G. Demirtaş, N. Dege, H. İçbudak, Ö. Yurdakul, O. Büyükgüngör, J. Inorg. Organomet. Polym. 22 (2012) 671–679.
[31] E. Aydemir, S. Kansiz, M.K. Gumus, N.Y. Gorobets, N. Dege, Acta Crystallographica Section E: Crystallographic Communications. 74 (2018) 367–370.
[32] S. Kansız, N. Dege, J. Mol. Struct. 1173 (2018) 42–51.
[33] S.D. Kanmazalp, M. Macit, N. Dege, J. Mol. Struct. 1179 (2019) 181–191.
[34] W. Guerrab, S. Ill-Min Chung, J.T. Kansiz, N. Mague, J. Dege, R. Taoufik, I. H. Salghi, M.I. Ali, H. Khan, Y.R. Lgaz, J. Mol. Struct. 1197 (2019) 369–376.
[35] D.J. Majumdar, J.E. Philip, A. Dubey, A. Tufail, S. Roy, Heliyon (2023) e16103.
[36] A. R. Guerroudj, N. Boukabcha, A. Benmohammed, N. Dege, N. El. H. Belkafouf, N. Khelloul, A. Djafri, A. Chouaih, J. Mol. Struct. 1240 (1-13) (2021) 130589.
[37] R. Ilmi, D. Zhang, J. D. L. Dutra, N. Dege, L. Zhou, W-Y. Wong, P. R. Raithby, M. S. Khan, Organic Electronics 96 (2021) 106216.
[38] Ö. Tamer, H. Mahmoody, K.F. Feyzioğlu, O. Kılınç, D. Avci, O. Orun, N. Dege, Y. Atalay, Appl. Organomet. Chem. 34 (3) (2020) 3–e5416.
[39] U. Ndagi, M.M. Lawal, M.E. Soliman, Russ. J. Phys. Chem. A 93 (2019) 1543–1558.
[40] M.M. Lawal, I.A. Lawal, M.J. Klink, G.F. Tolufashe, U. Ndagi, H. Kumalo, J. Inorg. Biochem. 206 (2020), 111044.
[41] V. H. Rezvana, Y. Aminivandb, https://dx.doi.org/10.2139/ssrn.4183399.
[42] A.M. Maharramov, K.T. Mahmudov, M.N. Kopylovich, A.J. Pombeiro, non-covalent interactions in the synthesis and design of new compounds, John Wiley & Sons, 2016.
[43] S. Bathula, M. Sankaranarayanan, B. Malgija, I. Kaliappan, R.R. Bhandare, A. B. Shaik, ACS Omega 8 (46) (2023) 44287–44311.
[44] SMART & SAINT Software Reference manuals Version 6.45; Bruker Analytical X-ray Systems, Inc.: Madison, WI, 2003.
[45] G. M. Sheldrick, SADABS, a software for empirical absorption correction, Ver.2.05; University of Göttingen: Göttingen, Germany, 2002.
[46] SHELXTL Reference Manual Ver. 6.1; Bruker Analytical X-ray Systems, Inc.: Madison, WI, 2000.
[47] G. M. Sheldrick, SHELXTL, a software for empirical absorption correction Ver.6.12; Bruker AXS Inc.: WI. Madison, 2001.
[48] A.L. Spek, PLATON, Utrecht University, Utrecht, Netherlands, A Multipurpose Crystallographic Tool, 2001.
[49] Y. Zou, S.K. Nair, Chemistry & Biology 16 (9) (2009) 961–970.
[50] R. Dennington, T. A. Keith, J. M. Millam, Gauss View 6.0. 16. Semichem Inc.: Shawnee Mission, KS, USA, 2016.
[51] A.D. Becke, J. Chem. Phys. 96 (3) (1992) 2155–2160.
[52] D. Vautherin, D.T. Brink, Phys. Rev. C. 5 (3) (1972) 626.
[53] E.G. Hohenstein, S.T. Chill, C.D. Sherrill, J. Chem. Theory Comput. 4 (12) (2008) 1996–2000.
[54] J. Bensalah, H. Ouaddari, S. Erdoğan, B. Tüzün, A.R. Gaafar, H.A. Nafidi, A. Habsaoui, Inorg. Chem. Commun. (2023), 111272.
[55] D. Ritchie, T. Orpailleur, Hex 8.0. 0 User Manual. Protein Docking Using Spherical Polar Fourier Correlations Copyright C, 2013.
[56] S. Salentin, S. Schreiber, V.J. Haupt, M.F. Adasme, M. Schroeder, PLIP: fully automated protein–ligand interaction profiler, Nucleic Acids Research 43 (W1) (2015) W443–W447.
[57] M.F. Adasme, K.L. Linnemann, S.N. Bolz, F. Kaiser, S. Salentin, V.J. Haupt, M. Schroeder, PLIP 2021: Expanding the scope of the protein–ligand interaction profiler to DNA and RNA, Nucl. Acids Res. 49 (W1) (2021) W530–W534.
[58] M.A. Spackman, D. Jayatilaka, CrystEngComm. 11 (2009) 19–32.
[59] F.L. Hirshfeld, Theor. Chem. Acta. 44 (1977) 129–135.
[60] H.F. Clausen, M.S. Chevallier, M.A. Spackman, B.B. Iversen, New J. Chem. 34 (2010) 193–199.
[61] A.L. Rohi, M. Moret, W. Kaminsky, K. Claborn, J.J. McKinnon, B. Kahr, Cryst. Growth Des. 8 (2008) 4517–4525.
[62] A. Parkin, G. Barr, W. Dong, C.J. Gilmore, D. Jayatilaka, J.J. McKinnon, M. A. Spackman, C.C. Wilson, CrystEngComm. 9 (2007) 648–652.
[63] P. Bhowmik, S. Chattopadhyay, M.G.B. Drew, C. Diaz, A. Ghosh, Polyhedron 29 (2010) 2637–2642.
[64] S. Chattopadhyay, M.G.B. Drew, A. Ghosh, Inorg. Chim. Acta. 359 (2006) 4519–4525.
[65] D. Sadhukhan, A. Roy, G. Rosair, L. Charbonniere, S. Mitra, BCSJ 84 (2011) 211–217.
[66] M. Amirnasr, K.J. Schenk, M. Salavati, S. Dehghanpour, A. Taeb, A. Tadjarodi, J. Coord. Chem. 56 (2003) 231–243.
[67] D.J. Majumdar, J.E. Philip, S. Roy, B. Tuzun, Results in Chemistry 4 (2022), 100574.
[68] B. Dutta, S. Paul, S. Halder, Heliyon 9 (2023) e13504.
[69] M.J. Turner, S. Grabowsky, D. Jayatilaka, M.A. Spackman, J. Phys. Chem. Lett. 5 (2014) 4249–4255.
[70] P. Venkatesan, S. Thamotharan, A. Ilangovan, H. Liang, T. Sundius, Spectrochim. Acta. Part A. 153 (2016) 625–636.
[71] M.J. Turner, S.P. Thomas, M.W. Shi, D. Jayatilaka, M.A. Spackman, Chem. Commun. 51 (2015) 3735–3738.
[72] G. Yuan, K.Z. Shao, D.Y. Du, X.L. Wang, Z.M. Su, J.F. Ma, CrystEngComm. 14 (2012) 1865–1873.
[73] U.O. Ozmen, B. Tuzun, E.B. Ayan, B.S. Cevrimli, J. Mol. Struct. 1286 (2023), 135514.
[74] F.S. Tokalı, P. Taslimi, B. Tüzün, A. Karakuş, N. Sadeghian, I. Gulçin, J. Ind. Chem. Soc. (2023) 1–12.
[75] A. Gannouni, W. Tahri, T. Roisnel, K. Riadh, J. Mol. Struct. 1271 (2023), 134094.
[76] R.G. Parr, L.V. Szentpaly, S. Liu, J. Am. Chem. Soc. 121 (9) (1999) 1922–1924.
[77] R. Parthasarathi, J. Padmanabhan, V. Subramanian, B. Maiti, P. hattaraj,, Chem. Phys. Letts. 394 (4–6) (2004) 225–230.
[78] R. Parthasarathi, J. Padmanabhan, V. Subramanian, B. Maiti, P. hattaraj,, Curr. Sci. (2004) 535–542.
[79] G. Mahalakshmi, V. Balachandran, SpectroChim. Acta. Part A. 135 (2015) 321–334.
[80] M.T. Riaz, M. Yaqub, Z. Shafiq, A. Ashraf, M. Khalid, P. Taslimi, R. Tas, B. Tuzun, İ. Gulçin, Bioorg. Chem. 114 (2021), 105069.
[81] L. Guo, Z.S. Safi, S. Kaya, W. Shi, B. Tüzün, N. Altunay, C. Kaya, Front. Chem. 6 (2018) 155.

[82] S. Hermi, M.H. Mrad, A.A. Alotaibi, B. Tüzün, U. Böhme, K.M. Alotaibi, C.B. Nasr, Inorg. Chem. Commun. 155 (2023), 111122.
[83] S. Selvakumari, K.M. Potla, D. Shanthi, A. Irfan, S. Muthu, J. Mol. Liq. 382 (2023), 121863.
[84] A. Mermer, B. Tüzün, S.D. Daştan, U.M. Koçyiğit, F.N. Çetin, O. Çevik, J. Biochem. Mol. Toxicol. (2023) e23465.
[85] M.S. Çelik, N. Kütük, A.F. Yenidünya, S. Çetinkaya, B. Tüzün, Biomass Convers. Biorefin. (2023) 1–12.
[86] A. Mermer, B. Tüzün, S.D. Daştan, O. Çevik, Polyhedron 242 (2023), 116487.
[87] R.B. Thurman, C.P. Gerba, G. Bitton, Crit. Rev. Environ. Sci. 18 (1989) 295–315.
[88] L. Macomber, J. A. Imlay, Proc. Natl. Acad. Sci. U S A. 106 (2009) 8344-8349.
[89] J.B. Fein, Q. Yu, J. Nam, N. Yee, Chemgeo. 521 (2019) 28–38.
[90] O.S. Pokrovsky, G.S. Pokrovski, L.S. Shirokova, A.G. Gonzalez, E.E. Emnova, Geobiology 10 (2012) 130–149.
[91] A. Frei, Metal complexes as antifungals? From a crowd-sourced compound library to the first in vivo experiments, ACS Au 2 (10) (2022) 2277–2294.
[92] N. Dharamaraj, P. Viswanathamurthi, K. Natarajan, Trans. Met. Chem. 26 (2001) 105–109.